



# Intermolecular interactions, spectroscopic and theoretical investigation of 4-aminoacetophenone

Mariana Rocha <sup>1</sup>, Alejandro Di Santo <sup>1</sup>, Aida Ben Altabef <sup>1</sup>, Diego M. Gil <sup>1\*</sup>

<sup>1</sup> INQUINOA (CONICET-UNT). Instituto de Química Física. Facultad de Bioquímica, Química y Farmacia. Universidad Nacional de Tucumán. San Lorenzo 456. T4000CAN. San Miguel de Tucumán. Argentina

\*Corresponding author E-mail: [dmgil@fbqf.unt.edu.ar](mailto:dmgil@fbqf.unt.edu.ar)

## Abstract

The molecular structure of 4-aminoacetophenone (PAAP) was determined by DFT calculations using different basis sets. The structural parameters, electronic properties and vibrational wavenumbers of the optimized geometry have been determined. The vibrational wavenumbers of the fundamental modes of the title compound have been precisely assigned and analyzed and the theoretical results are compared with the experimental vibrations observing a very good correlation. TD-DFT approach was applied to assign the electronic transitions observed in the experimental UV-vis spectrum. The molecular electrostatic potential map was used to identify the possible electrophilic and nucleophilic sites. Natural bond orbital (NBO) analysis and atoms in molecules (AIM) approach are applied in order to quantify the relative strength of hydrogen bonding interactions and to account their effect on the stabilities of molecular arrangements. In addition, a detailed exploration of the intermolecular interactions that stabilizes the crystal packing has been performed by using the Hirshfeld surface analysis.

**Keywords:** 4-Aminoacetophenone; NBO Analysis; Vibrational Spectra; Hirshfeld Surface Analysis; Intermolecular Interactions.

## 1. Introduction

The acetophenone compound is one of the most typical aromatic carbonyl and it is present naturally in a lot of foods including apple, cheese, apricot, banana and cauliflower and it shows interesting photochemical properties [1], [2]. It can be obtained by air oxidation of ethyl benzene, as a bi-product of cumen. Commercially significant resins are produced by reaction between acetophenone with formaldehyde and base. Acetophenone compounds are used in fragrances like almond, cherry, honeysuckle, jasmine and strawberry [3].

Acetophenones are compounds that exhibit interesting physicochemical and biological properties including antibacterial activity. A recent study has linked the antibacterial activity of twenty acetophenones with their structural characteristics by electronic and topological indices [4]. Balan and co-workers have reported that diazonium salts with dihydroxyacetophenone skeleton exhibit antimicrobial activity [5] and the complexes between p-substituted acetophenone and benzoylhydrazones present antifungal activity [6], [7]. Different flavonoids such as chalcones, flavones and flavanones are obtained by reaction between acetophenones and benzaldehydes, in alkaline medium [8], [9]. Substituted acetophenones are used as reagents for the synthesis of several organic reactions. Derivatives of acetophenone are precursors for conducting polymer and they are used as polymerization catalyst for the manufacture of olefins [10].

Medhi has reported the infrared (IR) and Raman spectra of the three isomeric acetophenones and presented a useful discussion on the assignments of different normal modes of vibration [11]. Gambi et al. have proposed the vibrational assignments of acetophenone and a number of its deuterated analogues (along with an NCA) on the basis of the IR spectrum [12]. Sett and co-workers have carried out a normal coordinate analysis of acetophenone employing a systematic procedure based on modified valence force field that is comparable to those used previously for different aromatic molecules [13].

In this contribution, we report the IR, Raman and UV-visible spectra measurements for para-aminoacetophenone. The experimental data were complemented with quantum chemical calculations. The molecular geometry optimizations were performed using DFT methods and different basis sets to assign the experimental IR and Raman spectra. The geometrical parameters computed were compared with those obtained by X-ray diffraction methods reported in literature. A detailed exploration of the intermolecular interactions that stabilized the crystal packing of the title compound have been performed using Hirshfeld surface analysis and their associated 2D Fingerprint plots. The reactivity of the molecule was evaluated by using the Natural Bond Orbital (NBO) analysis and the intramolecular and intermolecular interactions were studied using Atoms in Molecules (AIM) approach. UV-visible spectral analysis has also been used to elucidate the electronic transitions within the molecule in gas phase and in ethanol as solvent.

## 2. Experimental

The compound under study, para-aminoacetophenone (PAAP), was commercially supplied by Sigma–Aldrich and used without further purification.

### 2.1. Instrumentation

The FTIR spectrum of the compound in solid state was measured at room temperature (RT) in the region 4000–400  $\text{cm}^{-1}$  using a Perkin Elmer GX1 Fourier Transform infrared spectrometer. Figure 1 shows the IR and Raman spectra of the title compound in solid state. The Raman spectrum of the sample in solid state was recorded at RT in the 3500–50  $\text{cm}^{-1}$  interval on a ThermoScientific DXR Raman microscope. The Raman data were collected using a diode-pump, solid state laser of 532 nm (at 5  $\text{cm}^{-1}$  spectral resolution), a con-focal aperture of 25  $\mu\text{m}$  pinhole and 10X objective. To achieve a sufficient signal to noise ratio, 60 spectral scans of 6 s each were accumulated for the sample (laser power: 10 mW). The UV–visible spectrum was recorded between 800 and 200 nm using quartz cells (10 mm optical path length) on a Beckman/DU 7500 spectrophotometer in an ethanolic solution  $10^{-4}$  M of PAAP.

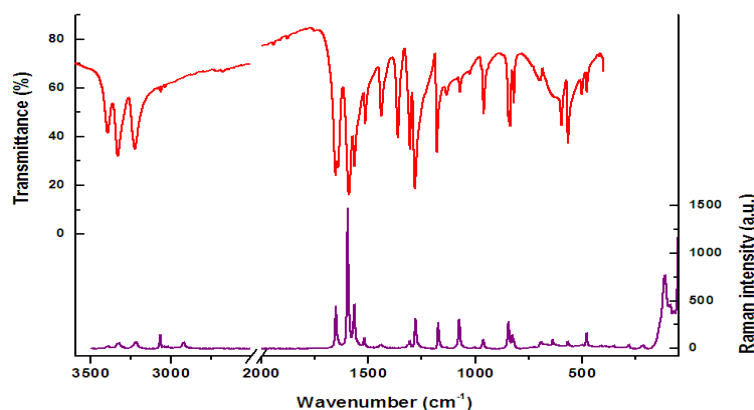


Fig. 1: Experimental IR and Raman Spectra for PAAP in Solid State.

### 2.2. Computational details

All quantum chemical calculations were performed with the Gaussian 03 program package [14]. The molecular geometries were optimized to standard convergence criteria by using DFT methods with Becke's three-parameter hybrid exchange functional [15] (B3) combined with both the Lee–Yang–Parr gradient-corrected correlation functional [16] (LYP). The calculations were carried out using 6-31G(d,p), 6-311+G(2d,p) and 6-311++G(d,p) basis sets. The calculated vibrational wavenumbers corresponded in all cases to potential energy minima for which no imaginary frequency was found. The vibrational modes were assigned by means of visual inspection using the Gaussview 05 program [17]. The potential energy distribution (PED) analysis was performed at B3LYP/6-311++G(d,p) level using the VEDA4 program [18]. In addition, an analysis of the reactivity and the evaluation of intra and intermolecular interactions of the compound was done within Bader's atoms in molecules theory (AIM) by using the AIM2000 code [19,20]. The natural bond orbital (NBO) calculation was performed at the B3LYP/6-311++G(d,p) level using the program NBO 3.1 [21]. This analysis were performed to understand various second order interactions between the filled orbitals of one subsystem and vacant orbitals of another subsystem, in order to have a measure of the intramolecular delocalization of hyper-conjugation. The electronic absorption spectra for the optimized structures were calculated in gas phase and with a single-electron approximation and the SCRF, Polarizable Continuum Model (PCM) approximation [22] in ethanol with the time dependent DFT (TD-DFT) at B3LYP/6-311++G(d,p) approximation. The molecular electrostatic potential surface (MEP) and electron density surface were also constructed using B3LYP/6-311++G(d,p) level.

### 2.3. Hirshfeld surface calculations

Hirshfeld surfaces and their associated 2D Fingerprint plots [23-25] have been performed using CrystalExplorer 3.0 software [26] using the .cif file obtained from the CCDC database. The  $d_{\text{norm}}$  (normalized contact distance) and the breakdown of the 2D fingerprint plots were used for decoding and quantifying the intermolecular interactions in the crystal lattice. The  $d_{\text{norm}}$  is a symmetrical function of distances to the surface from the nuclei inside and outside the Hirshfeld surface ( $d_i$  and  $d_e$ , respectively), relative to their respective van der Waals radii. A color scale of red (shorter than vdW separation)-white (equal to vdW separation)-blue (longer than vdW separation) was used to visualize the intermolecular interactions responsible of the crystal packing. Hirshfeld surfaces of the title compound were also mapped with shape index and curvedness properties. The 3D  $d_{\text{norm}}$  surfaces were mapped over a fixed color scale of -0.05 Å (red) to 0.95 Å (blue), the shape index in the color range of -1.0 a.u. (concave) to 1.0 a.u. (convex), and curvedness in the range of -4.0 a.u. (flat) to 4.0 a.u. (singular). The 2D fingerprint plots are displayed by using the translated 0.6-2.8 Å range, and including reciprocal contacts.

## 3. Results and discussion

### 3.1. Molecular geometry

The molecular structure were optimized using B3LYP method with 6-31G(d,p), 6-311+G(2d,p) and 6-311++G(d,p) basis sets. Figure 2 shows the optimized molecular structure calculated at B3LYP/6-311++G(d,p) approximation. The structural parameters obtained by calculations were compared with those experimental data reported previously from single-crystal X-ray crystallography [27]. Table 1 shows the calculated structural parameters at different levels of theory compared with the experimental ones, showing a very good agreement between them. Theoretical calculations demonstrated that the most stable conformer is exactly planar where the dihedral angles O(15)-

C(14)-C(4)-C(3) and O(15)-C(14)-C(4)-C(5) are  $-179.7^\circ$  and  $0.248^\circ$ , respectively computed at B3LYP/6-311++G(d,p) approximation. The calculated and observed bond lengths and angles are consistent with the description of the molecular structure in terms of formally single, double and resonant bonds. The influence of the substituent on the molecular parameters, particularly in the C-C bond lengths of the ring carbon atoms seems to be small. The average bond lengths C-C of the aromatic ring is  $1.398 \text{ \AA}$  at B3LYP/6-311++G(d,p) level. The longer bond length ( $1.488 \text{ \AA}$ ) of C(4)-C(14) is due to the absence of delocalization of the carbonyl lone pair of electrons towards the ring. Similarly, the bond length C(14)-C(16) is  $1.52 \text{ \AA}$  because of the hyper-conjugative effect of the methyl group and due to the partial ionic character of the C=O group, decreases in force constant and increase the bond length compared with molecules that contain only hydrogen in the structure. The C-N bond length is shorter than the average single C-N bond length ( $1.472 \text{ \AA}$ ). This result is in accordance with the expected delocalization in the molecule and confirmed by the bond angle C-N-H of  $117.3^\circ$  showing a  $sp^2$  hybridization on N (11).

The dipole moment of PAAP calculated at B3LYP method and different basis sets are shown in Table 1. The higher value was observed for the B3LYP/6-311++G (d, p) approximation. The high values observed for this compound are due to the inductive influence of the  $\text{NH}_2$  group in the para-position (See Fig. S1, Supplementary Information).

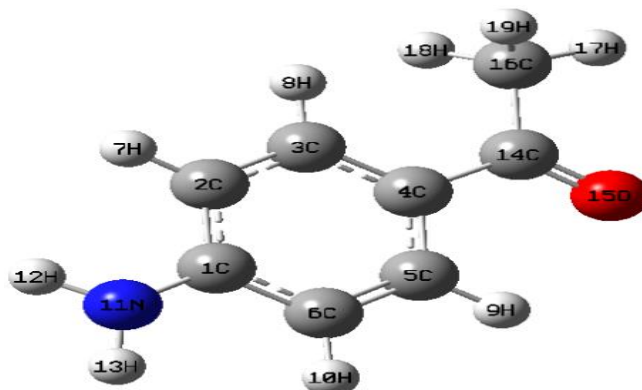


Fig. 2: Optimized Molecular Structure of PAAP at B3LYP/6-311++G (d, p) approximation.

Table 1: Structural Parameters (Bond Lengths, Angles and Dihedral Angles) for PAAP Calculated at B3LYP Level with Different Basis Sets

Parameters <sup>a</sup>	B3LYP			Experimental <sup>b</sup>
	6-31G (d, p)	6-311+G (2d, p)	6-311++G (d, p)	
Bond lengths (Å)				
C16-H	1.094	1.091	1.092	0.920
C14-C16	1.522	1.518	1.520	1.498
C14-O15	1.224	1.219	1.220	1.215
C14-C4	1.488	1.486	1.488	1.468
C4-C5	1.406	1.402	1.405	1.390
C5-C6	1.384	1.379	1.382	1.370
C6-C1	1.410	1.405	1.408	1.399
C1-N11	1.385	1.386	1.385	1.376
C1-C2	1.408	1.402	1.405	1.398
C2-C3	1.388	1.384	1.387	1.369
C3-C4	1.405	1.399	1.403	1.396
Angles (°)				
C16-C14-O15	120.1	119.1	120.1	119.2
O15-C14-C4	121.1	121.1	121.1	120.1
C16-C14-C4	118.9	118.9	118.8	120.7
C14-C4-C5	118.6	118.9	118.9	119.7
C4-C5-C6	121.4	121.3	121.4	122.3
C5-C6-C1	120.4	120.5	120.5	120.3
C6-C1-N11	120.7	120.6	120.6	120.9
C1-C2-C3	120.5	120.5	120.5	120.5
C2-C3-C4	121.2	121.3	121.3	122.1
C3-C4-C14	123.5	123.2	123.2	123.6
Dihedral angles (°)				
C16-C14-C4-C5	-178.9	-179.7	-179.7	-
C16-C14-C4-C3	0.312	0.325	0.332	-
O15-C14-C4-C3	-179.7	-179.7	-179.7	-
O15-C14-C4-C5	0.196	0.245	0.248	-
C14-C4-C5-C6	-179.9	-179.9	-179.3	-
C14-C4-C3-C2	179.8	179.9	179.9	-
C4-C5-C6-C1	0.011	0.092	0.088	-
C3-C2-C1-N11	177.5	177.4	177.6	-
C5-C6-C1-N11	-177.6	-177.5	-177.7	-
Dipole moment (Debye)	4.894	4.970	5.047	-

<sup>a</sup> For atoms numbering, see Fig. 2; <sup>b</sup> The experimental data reported in Ref. [27].

### 3.2. NBO, topological (AIM) and MEP analysis

The natural bond orbital (NBO) calculations have been performed to evaluate energetically the hyper-conjugative and conjugative interactions that stabilize the structure of the title compound. NBO analysis is a useful tool for understanding delocalization of electron density from occupied Lewis-type (donor) NBOs to properly unoccupied non-Lewis type (acceptor) NBOs within the molecule. The stabilization energy  $E^{(2)}$  associated with donor (i) and acceptor (j) delocalization is estimated from the second-order perturbation theory as follow [21]:

$$E^{(2)} = q_i \frac{F^2(i,j)}{\varepsilon_j - \varepsilon_i} \quad (1)$$

Where  $q_i$  is the donor orbital occupancy,  $\varepsilon_i$  and  $\varepsilon_j$  are diagonal elements (orbital energies) and  $F(i, j)$  is the off-diagonal Fock matrix element. The large value of  $E^{(2)}$  indicates an intense interaction between electron donors and electron acceptors. The NBO calculations were performed at B3LYP/6-311++G(d,p) level of theory. The most relevant interactions determined by means the NBO analysis are presented in Table 2. The hyper-conjugative interactions are formed by the orbital overlap between  $\pi$  (C-C) bond orbital to  $\pi^*$  (C-C) anti-bonding orbital, which results in intra-molecular charge transfer causing the stabilization of the system. These interactions can be identified by finding the increase in electron density in the anti-bonding orbital. The strong intra-molecular hyper-conjugation interaction of the  $\pi$  electrons of the C-C to anti C-C and C-O bond in the ring leads to stabilization of some part of the ring as can be shown in Table 2. The lone pair LP O(15) participates in LP O(15)  $\rightarrow$   $\sigma^*$ C(4)-C(14) and LP O(15)  $\rightarrow$   $\sigma^*$ C(14)-C(16) interactions with energies of 20.17 and 21.49 kcal mol<sup>-1</sup>, respectively. A strong interaction has been observed between the lone electron pair LP N(11) and the  $\pi^*$ C(1)-C(2) with an energy of 31.01 kcal mol<sup>-1</sup>. This electron donation into the  $\pi^*$ C(1)-C(2) anti-bonding orbital is reflected in the high population found for this "vacant" molecular orbital, with an electron occupancy of 0.41e. This result suggests a partial double bond character in the N(11)-C(1) bond as was reflected in the shorter bond length C-N compared with a single bond. Higher LP<sub>p</sub> (N)  $\rightarrow$   $\pi^*$  C-C interaction values are associated with shorter C-N bond lengths.

The NBO analysis has been also performed to investigate the relative strength of a hydrogen bonded dimer. The optimized structure of a dimer obtained from the crystal structure is shown in Figure S2. The oxygen/nitrogen atom with lone pair acts as donor and N-H as acceptor in the strong intermolecular charge transfer interaction. For the compound under study, the stabilization energy  $E^{(2)}$  associated with the hyper-conjugative interaction LP O15  $\rightarrow$   $\sigma^*$  N-H is obtained as 8.73 kcal mol<sup>-1</sup>. Similar results were obtained for acyl-substituted hydrazones with a computed value of stabilization energy of 9.88 kcal mol<sup>-1</sup> [28].

The total atomic charges of PAAP are obtained from natural population analysis (NPA) computed at B3LYP/6-311++G(d,p) level (see Table S1, Supplementary Information). The atomic charges obtained using NPA revealed that the more negative charge (-0.77692 a.u.) is located over N(11) atom of the amino group and the negative charge (-0.57498 a.u.) is located at O(15) atom. The more negative charge on O(15) makes C(14) atom more positive and acidic (charge: +0.55170 a.u.). The negative charges mainly located on N(11) and O(15) atoms indicate that these atoms could interact with the positive part of a receptor. In addition, C(14) atom is the most positive charged part and this atom could interact with the negatively charged part of a receptor easily.

The quantum theory of atoms in molecules has been useful in the characterization of bonds through a topological analysis of the electronic charge density and their Laplacian at the Bond Critical Point (BCP) [29]. In the AIM theory the nature of the bonding interaction can be determined through an analysis of the properties of the charge density,  $\rho$ , and its Laplacian  $\nabla^2(\rho)$  at the BCP, and through the properties of the atoms, which are obtained by integrating the charge density over the atom orbitals [29]. The molecular graph of the title compound using AIM program calculated at B3LYP/6-311++G(d,p) approximation is presented in the Supplementary Information (Figure S3). Table 3 shows the bond critical point data for PAAP. The value of charge density for C(14)=O(15), C(4)-C(14), C(1)-N(11) and C(14)-C(16) bond critical points are larger and the Laplacian electron density are positive, except for C(14)=O(15). Analyzing the sign of the Laplacian, one can define the regions where the charge density is concentrated ( $\nabla^2(\rho) < 0$ ) or depleted ( $\nabla^2(\rho) > 0$ ). The results shown in Table 3 indicate that the charge density has been concentrated in the inter-nuclear region for C(4)-C(14), C(1)-N(11) and C(14)-C(16). The large and positive value of the Laplacian for C(14)=O(15) indicates that the electronic charge is depleted between the nuclei. These results are in accordance with those reported by Roohi et al [30] and with calculations performed for different kinds of molecules studied in our group [31-33]. The AIM theory is a very useful tool in analyzing the intra and intermolecular hydrogen bonds. The formation of hydrogen bonds is associated to the presence of a bond critical point (BCP) between the hydrogen atom of donor group and acceptor atom which are linked by the associated bond path. The molecular graph of the molecular dimer using AIM2000 package is shown in Figure S4 (Supplementary Information). The BCP between oxygen and hydrogen confirms that there is an intermolecular hydrogen bond in these molecules. The theoretical results confirming the presence of intermolecular N-H...O(keto) hydrogen bonds. Koch and Popelier propose a set of criteria for the existence of hydrogen bonding within the AIM approach [34]. In accordance with these criteria, the value of electron density ( $\rho$ ) at the BCP of H...A lies in the range 0.002-0.04 a.u. and the corresponding Laplacian of electron density at the BCP is within the range 0.024-0.139 a.u. For the title compound, the obtained electron density and its Laplacian at the BCP for the N-H...O hydrogen bond were 0.02037 a.u. and 0.06796 a.u., respectively. The low values of density and positive values of its Laplacian at the BCP indicate the presence of significant hydrogen bonding interactions. The energy of N-H...O hydrogen bond can be calculated using the formula described by Espinosa and co-workers [35] that proposed a proportionality between hydrogen bond energy  $E_{HB}$  and potential electron energy density at H...O bond critical point  $V(r_{BCP})$ ,  $E_{HB} = V(r_{BCP})/2$ . In case of PAAP,  $E_{HB}$  has been calculated to be 5.023 kcal mol<sup>-1</sup> at B3LYP/6-311++G(d,p) level. Two topological parameters such as total electron energy density  $H_{BCP}$  and Laplacian of electron density at the BCP are useful in characterization of the strength of hydrogen bonds. In accordance to the criteria proposed by Rozas and co-workers [36], the interactions can be classified as follow: a) weak hydrogen bonds are characterized by  $\nabla^2(\rho) > 0$ ,  $H_{BCP} > 0$  and  $E_{HB} < 12$  kcal mol<sup>-1</sup>; b) medium hydrogen bonds are characterized by  $\nabla^2(\rho) > 0$ ,  $H_{BCP} < 0$  and  $E_{HB}$  in the range 12-24 kcal mol<sup>-1</sup>; c) strong hydrogen bonds are characterized by  $\nabla^2(\rho) < 0$ ,  $H_{BCP} < 0$  and  $E_{HB} > 12$  kcal mol<sup>-1</sup>. Based in our calculations, the  $H_{BCP}$  of the N-H...O hydrogen bond is 0.0155 a.u. indicating weak hydrogen bonding interactions.

The molecular electrostatic potential (MEP) was used in order to understand the sites of electrophilic and nucleophilic attacks for the title compound [37, 38]. The color code originates from red and terminates with blue color. The red color represents the highest negative potential sites while the blue color represents the highest positive potential sites. The green color represents the sites with zero potential. The MEP plot for the title compound generated at the optimized geometry is shown in the Supplementary Information (Figure S5). The red region is mainly located on the oxygen atom of the carbonyl group. The atomic charge analysis and MEP calculations confirmed that the carbonyl oxygen atom is preferred site for electrophilic attack. It is evident from the MEP map that the region around the hydrogen atoms of the amino group is electron deficient (blue region), indicating that this region is very susceptible to nucleophilic attack. These results are in accordance with NPA charges with maximum positive values +0.37787 and +0.37851 a.u. for H(12) and H(13) atoms, respectively.

**Table 2:** Second-Order Perturbation Theory Analysis of the Fock Matrix for 4-Aminoacetophenone Calculated by the NBO Method at B3LYP/6-311++G (d, p) Approximation

Interaction (donor-acceptor) <sup>a</sup>	E <sup>(2)</sup> <sup>b</sup> (kcal mol <sup>-1</sup> )	E(j)-E(i) <sup>c</sup> (a.u.)	F(i,j) <sup>d</sup> (a.u.)
$\pi$ C1-C2 $\rightarrow$ $\pi^*$ C5-C6	13.63	0.29	0.058
$\pi$ C1-C2 $\rightarrow$ $\pi^*$ C3-C4	26.43	0.29	0.078
$\pi$ C3-C4 $\rightarrow$ $\pi^*$ C1-C2	16.48	0.27	0.060
$\pi$ C3-C4 $\rightarrow$ $\pi^*$ C5-C6	22.41	0.28	0.072
$\pi$ C3-C4 $\rightarrow$ $\pi^*$ C14-O15	20.51	0.28	0.071
$\pi$ C5-C6 $\rightarrow$ $\pi^*$ C1-C2	23.55	0.27	0.074
$\pi$ C5-C6 $\rightarrow$ $\pi^*$ C3-C4	14.79	0.29	0.060
LP O15 $\rightarrow$ $\sigma^*$ C4-C14	20.17	1.83	0.149
LP O15 $\rightarrow$ $\sigma^*$ C14-C16	21.49	1.70	0.147
LP N11 $\rightarrow$ $\pi^*$ C1-C2	31.01	0.32	0.094

<sup>a</sup> See Fig. 2 for atoms numbering scheme. LP denotes lone pair of electrons on the specified atom.

<sup>b</sup> E<sup>(2)</sup> means energy of hyper-conjugative interactions.

<sup>c</sup> Energy difference between i (donor) and j (acceptor) NBO orbitals.

<sup>d</sup> Fock matrix element I and j NBO orbitals.

**Table 3:** Bond Critical Point (BCP) Data and BCP Distances (In A.U.) to Attractors Calculated at B3LYP/6-311++G (d, p) Level Using AIM Analysis

Bond (X-Y) <sup>a</sup>	$\rho$ <sup>b</sup>	$\nabla^2(\rho)$ <sup>b</sup>	BCP-X	BCP-Y	Bond length (Å)
C (4) =O (15)	0.3982	0.1979	0.7631	1.5516	1.224
C (4)-C (14)	0.2702	-0.6684	1.3898	1.4218	1.488
C (1)-N (11)	0.3078	-0.9736	0.9497	1.6682	1.385
C(14)-C (16)	0.2543	-0.6084	1.4605	1.4163	1.522

<sup>a</sup> See Fig. 2 for atoms numbering. The first and second atom to the Bond Critical Point (BCP).

<sup>b</sup> Values in a.u.

### 3.3. Hirshfeld surface analysis

Molecular Hirshfeld surfaces in the crystal structure are constructed taking into account the electron distribution calculated as the sum of spherical atom electron densities [23-25]. The Hirshfeld surface enclosing a molecule is defined by points where the contribution of the electron density from the molecule of interest is equal to the contribution from all the other molecules. For each point on that isosurface, two distances are defined; one of them is  $d_e$  (the distance from the point to the nearest nucleus external to the surface) and  $d_i$  (the distance to the nearest nucleus internal to the surface). The normalized contact distance ( $d_{norm}$ ) based on both  $d_e$  and  $d_i$  and the van der Waals (vdW) radii of the atom (equation 2) enables identification of the regions of particular importance to the intermolecular interactions [23-25]. A color scale of red (shorter than vdW separation)- white (equal to vdW separation)-blue (longer than vdW separation) was used to visualize the intermolecular contacts.

$$d_{norm} = \frac{d_i - r_i^{vdW}}{r_i^{vdW}} + \frac{d_e - r_e^{vdW}}{r_e^{vdW}}$$

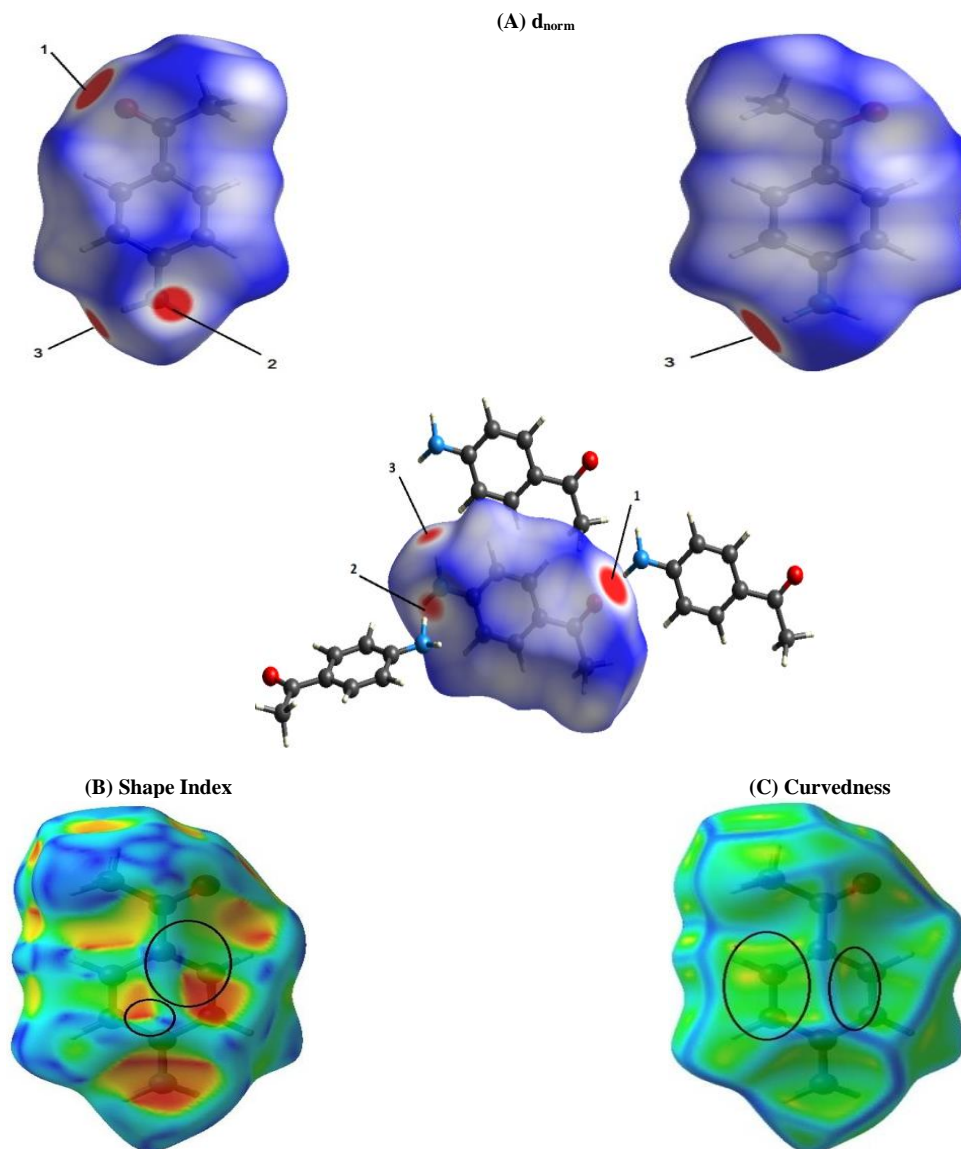
In accordance with the crystal structure of the title compound previously reported [27], the supramolecular assembly is characterized for different types of hydrogen bonding interactions. Figure 3 shows surfaces mapped over  $d_{norm}$ , Shape Index and Curvedness properties for PAAP. The deep red areas labeled 1 and 3 in the  $d_{norm}$  map indicate H...O(keto) contacts, attributable to N-H...O(keto) hydrogen bonds. The deep red region labeled 2 in the  $d_{norm}$  surface suggests N...H interactions due to H...N-H hydrogen bonds, where the lone pair electrons of N atom interacts with the H atom of the amino group of another molecule. The crystal packing of the title compound exhibits an interesting intermolecular pattern characterized by different structural motifs, being most relevant the formation of  $R_4^2(20)$  rings (See Figure 4a). Table 4 shows the geometrical parameters of the intermolecular hydrogen bonds of the structure of the title compound, indicating the presence of strong hydrogen bonds forming a pattern graph set C (8), giving rise a polymeric arrangement (See Fig. 4b).

The supramolecular assembly of PAAP also includes the existence of  $\pi$ -stacking interactions with offset or slipped facial arrangement involving the phenyl ring of one molecule and the phenyl ring of another molecule (See Fig. 4c). The patterns of complementary red and blue triangles observed in the shape index are indicative of  $\pi$ - $\pi$  interactions (showed in the highlighted circles in Fig 3b). The red triangles are concave regions associated with atoms of the  $\pi$ ... $\pi$  stacked rings above them, while the blue triangles are convex regions indicating the aromatic ring atoms of the molecule inside the surface. The existence of  $\pi$ - $\pi$  interactions in the title compound is also evident because relatively large and green flat regions delineated by circles in the Curvedness map are observed. The inter-centroid Cg(1) ... Cg(1) distances of 5.180 Å suggest the existence of weak  $\pi$ - stacking contacts, with offset facial arrangement (See Fig. 4c).

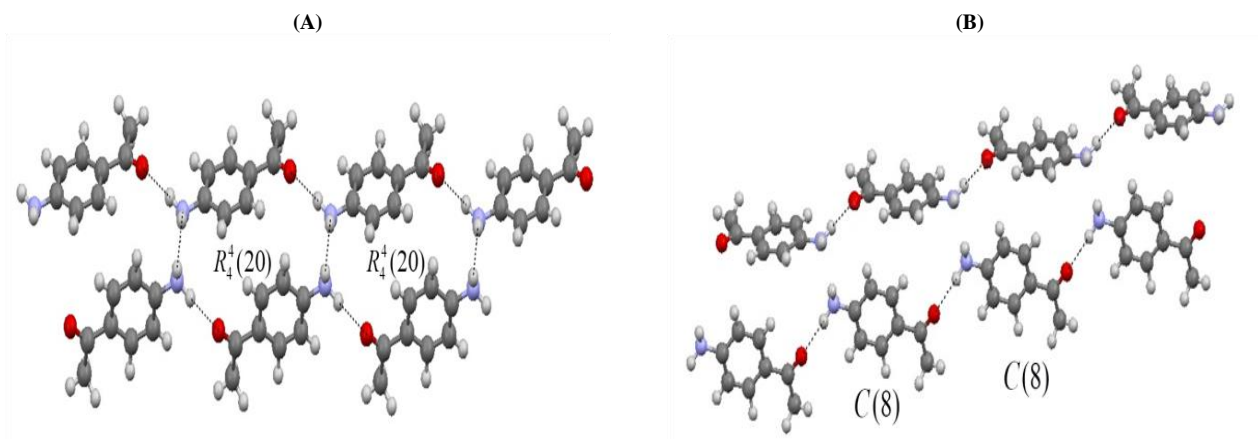
Two dimensional (2D) fingerprint plots were obtained by calculating the distances from the Hirshfeld surface to the nearest nucleus inside the surface ( $d_i$ ) to the outs of surface ( $d_e$ ) to analyze the molecular interaction around the nearest neighbor molecules. In 2D plots, green regions show closer contacts and blue color indicates longer contacts. Complementary regions are visible in the fingerprint plots where one molecule acts as donor ( $d_e > d_i$ ) and the other as acceptor ( $d_e < d_i$ ). The decomposed 2D fingerprint plots for the main intermolecular interactions of the title compound are shown in Figure 5. The shortest contacts located in the middle of scattered points in 2D fingerprint map ( $d_e+d_i \approx 2.5$  Å) are attributed to H...H contacts with a 48.2% of contribution, as result of the high content of H atoms in the molecule. The C...H/H...C interactions appear in a characteristic way for C-H... $\pi$  interactions, with a  $d_e+d_i$  at around 2.9 Å. These contacts represent 29.4% of the total Hirshfeld surface area. These interactions could be observed in the  $d_{norm}$  plot as white areas over the carbon atoms. The pair of narrow pointed spikes around  $d_e+d_i$  of 2.25 Å show the presence of O...H/H...O contacts (17.6% of contribution). Finally, the N...H/H...N contacts are represented by spikes near  $\approx 2.5$  Å in the fingerprint plot and comprise 4.9% of total Hirshfeld surface area. This study emphasizes the importance of Hirshfeld surfaces and their fingerprint plots for a full understanding of non-classical hydrogen bonds and short intermolecular contacts not easily visible in the crystal structure investigation.

Enrichment ratio was calculated from Hirshfeld surface in order to analyze the propensity of two chemical species (XY) to be in contact. The enrichment ratio establishes a relationship between the real contacts in the crystal packing with random contacts, calculated as if all kind of contacts had the same probability to form [39]. The enrichment ratio  $E_{XY}$  of a pair of elements X, Y is defined as a ratio between the proportion of actual contacts in the crystal ( $C_{XY}$ ) and the theoretical proportion of random contacts ( $R_{XY}$ ). The proportion  $S_X$  of Hirshfeld surface contacts involving the pair of elements X and Y is obtained from  $C_{XX}$  and  $C_{XY}$  values. The random contacts  $R_{XY}$  could be obtained by the probability products of  $S_X$  and  $S_Y$  proportions. For contacts with the same polarity we expected values lower than 1, which means a

low propensity to form contact, while values of  $E_{XY}$  larger than unity of pair of elements indicates a high propensity to form contacts in the crystal. The enrichment ratios of the main intermolecular interactions for PAAP are listed in the Supplementary Information (Table S2). The  $E_{NH}$  and  $E_{OH}$  for the  $N\cdots H$  and  $O\cdots H$  hydrogen bonds show values larger than unity indicating that these elements have high propensity to form contacts in the crystal lattice. On the other hand, the  $H\cdots H$  contacts can be considered as favored due to its  $E_{HH}$  that is near to unity ( $E_{HH} = 0.87$ ).



**Fig. 3:** Hirshfeld Surfaces Mapped Over A)  $d_{norm}$ ; B) Shape Index and C) Curvedness Properties for PAAP.



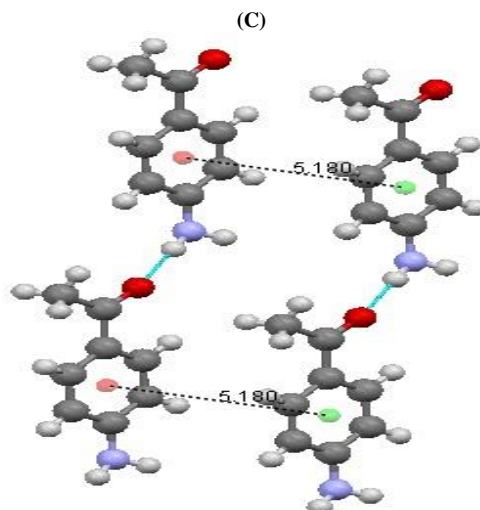


**Fig. 4:** Packing Diagram of PAAP Showing Intermolecular (A) N-H...O(Keto) and N-H...N Hydrogen Bonds as Dashed Lines, (B) N-H...O(Keto) Hydrogen Bonds Forming A Polymeric Arrangement And (C)  $\pi$ -Stacking Interactions Between Phenyl Rings.

**Table 4:** Hydrogen Bonds Geometrical Parameters for PAAP, Obtained from Ref. [27].

D-H...A	d(D-H)	d(H...A)	d(D...A)	$\angle$ (D-H...A)
Intermolecular				
N-H...N1 <sup>i</sup>	0.90	2.38	3.2170(6)	154
N1-H...O1 <sup>ii</sup>	0.94	1.97	2.9050(6)	177

Symmetry codes: (i)  $x, y, 1+z$ ; (ii)  $1/2-x, 1/2+y, 2-z$ .

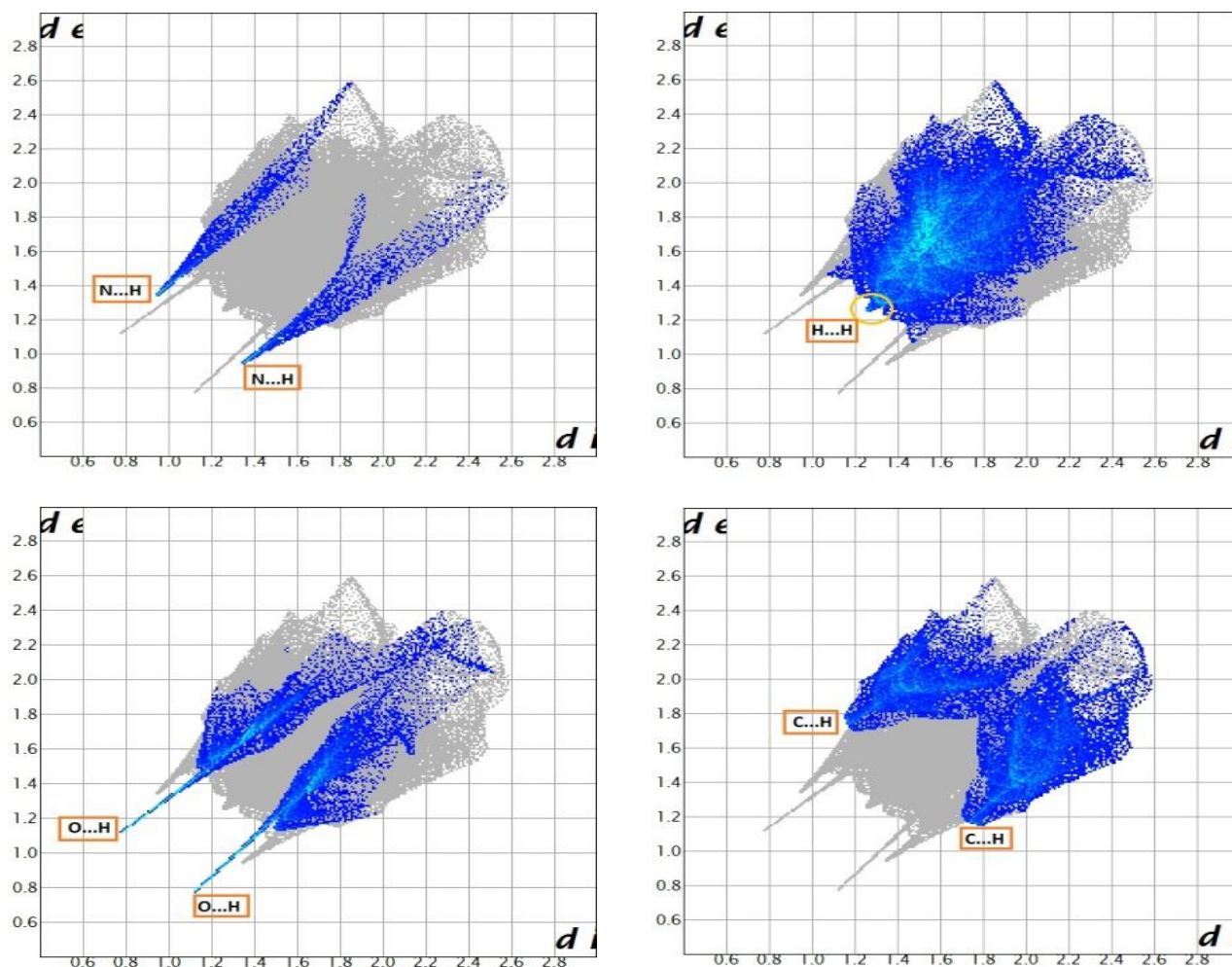


**Fig. 5:** Decomposed 2D Fingerprint Plots Derived from the Hirshfeld Surfaces of PAAP.

### 3.4. Electronic spectra and frontier molecular orbitals

The experimental and calculated electronic absorption spectra of the title compound are shown in Figure 6. Table 5 shows the main absorption bands, correlated with the computed values and a tentative assignment of the electronic transitions. A good agreement between experimental and computed electronic absorption spectra was observed. The electronic spectrum in ethanol shows an intense band located at 320 nm and a shoulder at 301 nm. In accordance with the values of oscillator strengths, the band located at 320 nm in the experimental electronic spectra is assigned to an electron promotion from HOMO to LUMO molecular orbitals with 97% of contribution ( $\pi \rightarrow \pi^*$  nature). The frontier molecular orbitals mainly involved in the electronic transitions are plotted in Figure 7. As shown in Figure 7, the HOMO corresponds to a  $\pi$  bonding system localized over phenyl ring and p-type orbitals strongly located on the oxygen atom of the carbonyl group and on the N atom of the amino group. The LUMO exhibits  $\pi$  anti-bonding character delocalized over the carbon atoms of the phenyl rings and non-bonding character of N atom of the amino group and the oxygen of carbonyl. The energy between HOMO and LUMO frontier molecular orbitals is an important parameter in determining the reactivity of the compounds [40-42]. The energy gap HOMO-LUMO was predicted to be 4.465 eV obtained at B3LYP/6-311++G(d,p) level, indicating that the title compound is stable. The shoulder observed at 301 nm in the experimental spectrum is attributed to one-electron transitions from HOMO to LUMO+1 (60%) and to minor contributions of HOMO-2  $\rightarrow$  LUMO (40%). Both transitions are of  $\pi \rightarrow \pi^*$  nature. The HOMO-1 molecular orbital principally involves the non-bonding character of the oxygen and carbon atoms of the acetyl group, while the HOMO-2 presents the contribution of the  $\pi$ -bonding character of the double bonds of the phenyl ring.

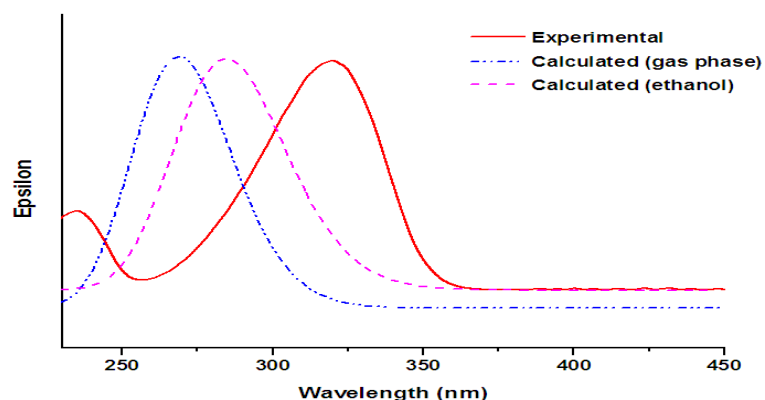


Fig. 6: Experimental and Theoretical (Gas Phase and Ethanol) UV-Visible Spectra.

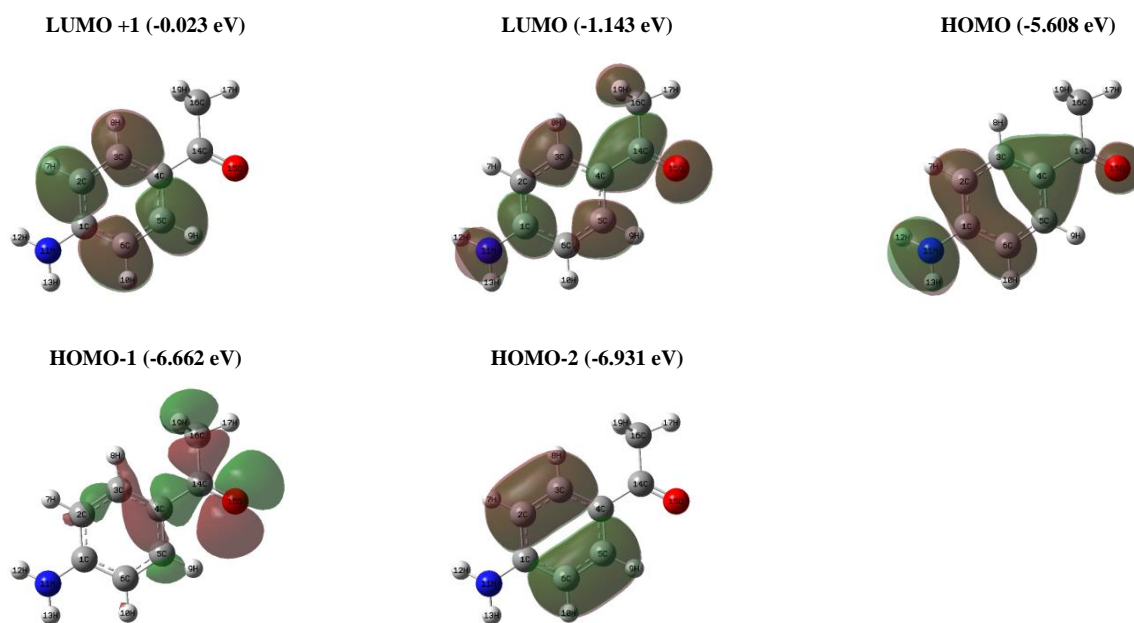


Fig. 7: Frontier Molecular Orbitals Involved in the Electronic Transitions of PAAP.

### 3.5. Vibrational properties

A tentative assignment of the 51 vibrational modes expected for the title compound is listed in Table 6. The analysis of the experimental IR and Raman spectra of the solid sample of PAAP (see Fig. 1) was supported by theoretical calculations using B3LYP/6-311++G(d,p) approximation. Figures 8 and 9 show graphical comparisons between the experimental and theoretical spectra obtained for the title compound. Zhou and co-workers demonstrated that scaled B3LYP calculations are powerful approaches for understanding the vibrational spectra of medium-sized organic compounds and the recommended factor of 0.96 was used to scale the theoretical frequencies [43]. The title compound consists of a benzene ring substituted with an acetyl group and an amino group in para position with regard to that group; the vibrational modes are therefore grouped and discussed as: a)  $\text{NH}_2$  group vibrations; b) acetyl vibrations (methyl and carbonyl); c) Ring vibrations.

**Table 6:** Experimental and Calculated Frequencies (in  $\text{cm}^{-1}$ ) and Tentative Assignments of the Fundamental Modes for 4-Aminoacetophenone.

Experimental	Calculated <sup>c</sup>	IR intensity	Raman activity	Tentative assignment (PED %) <sup>d, e</sup>		
IR <sup>a</sup>	Raman <sup>b</sup>	Unscaled	Scaled			
3332 m	3329 (4)	3688	3540	24	66	$\nu_a \text{NH}_2$ (100)
3226 m	3220 (5)	3584	3441	51	303	$\nu_s \text{NH}_2$ (100)
-	-	3197	3069	3	88	$\nu \text{C5-H}$ (96)
3064 vvw	3067 (10)	3188	3060	8	88	$\nu \text{C3-H}$ (89)
-	-	3159	3033	18	94	$\nu \text{C6-H}$ (83)
3048 vvw	3047 (2)	3159	3033	12	98	$\nu \text{C2-H}$ (78)
-	-	3140	3014	14	95	$\nu_a \text{CH}_3$ (94)
2977 vvw	-	3089	2965	10	45	$\nu_a \text{CH}_3$ (100)
-	2921 (5)	3032	2911	4	171	$\nu_s \text{CH}_3$ (95)
1652 s	1651 (31)	1729	1660	213	118	$\nu \text{C=O}$ (85)
1641 s	1641 sh	1663	1596	282	88	$\delta \text{NH}_2$ (43) + $\nu \text{C5-C6}$ (27)
1589 vs	1596 (100)	1642	1576	205	190	$\nu \text{C5-C6}$ (31) + $\delta \text{NH}_2$ (40)
1564 m	1564 (31)	1604	1540	26	10	$\nu \text{C2-C1}$ (60) + $\delta \text{CCH}$ (14)
1514 m	1518 (8)	1544	1482	15	20	$\delta \text{CCH}$ (45) + $\delta \text{CCC}$ (16)
1439 w	1443 (3)	1482	1423	11	9	$\delta_a \text{CH}_3$ (77)
-	1434 sh	1472	1413	12	5	$\delta_a \text{CH}_3$ (71)
-	-	1467	1408	23	6	$\nu \text{C2-C3}$ (39) + $\delta \text{CCH}$ (31)
1361 m	-	1387	1332	61	1	$\delta_s \text{CH}_3$ (86)
1305 m	1306 (6)	1363	1308	1	<1	$\nu \text{C2-C3}$ (32) + $\nu \text{C14-C16}$ (20) + $\delta \text{CNH}$ (12)
-	-	1334	1281	16	3	$\delta \text{CCH}$ (57)
1281 s	1279 (22)	1318	1265	78	9	$\nu \text{C1-N11}$ (51) + $\delta \text{CCH}$ (24)
1178 m	1172 (9)	1288	1236	277	57	$\nu \text{C4-C14}$ (51)
1133 w	1137 (1)	1200	1152	117	19	$\delta \text{CCH}$ (74) + $\nu \text{C5-C6}$ (17)
1085 vvw	-	1152	1106	10	1	$\delta \text{CCH}$ (56) + $\nu \text{C2-C3}$ (20)
1072 w	1074 (21)	1090	1046	4	42	$\nu \text{C14-C16}$ (28) + $\delta \text{CCO}$ (13) + $\rho \text{CH}_3$ (22)
1025 vw	-	1072	1029	2	2	$\rho \text{NH}_2$ (59)
-	-	1043	1001	1	<1	$\rho \text{CH}_3$ (38) + $\gamma \text{C=O}$ (28) + $\delta_a \text{CH}_3$ (19)
960 m	963 (7)	1023	982	<1	2	$\delta \text{CCC}$ (66) + $\delta \text{CCO}$ (13)
-	-	993	953	1	<1	$\gamma \text{C5-H}$ (77)
-	-	956	918	2	<1	$\rho \text{CH}_3$ (34) + $\nu \text{C14-C16}$ (31) + $\delta_a \text{CH}_3$ (11)
874 vvw	-	955	917	48	12	$\gamma \text{C2-H}$ (75)
844 m	845 (20)	846	812	17	30	$\nu \text{C1-C2}$ (40) + $\delta \text{CCC}$ (12)
836 m	-	841	807	34	15	$\gamma \text{C6-H}$ (69)
819 w	825 (10)	819	786	9	<1	$\gamma \text{C2-H}$ (83)
-	-	739	709	<1	1	$\tau \text{C5-C5-C4-C3}$ (68)
696 vw	692 (5)	696	668	2	4	$\nu \text{C14-C16}$ (53) + $\delta \text{CCC}$ (20)
-	639 (7)	652	626	1	6	$\delta \text{CCC}$ (69) + $\nu \text{C1-C2}$ (10)
596 w	-	597	573	14	<1	$\gamma \text{C14-C16-C4-O15}$ (47) + $\rho \text{CH}_3$ (24)
566 m	567 (5)	577	554	20	2	$\delta \text{C16C14O15}$ (60)
501 vw	502 (3)	507	487	26	2	$\gamma \text{CCCN}$ (70)
478 vvw	479 (12)	470	451	11	3	$\omega \text{NH}_2$ (67)
-	415 (2)	453	435	366	17	$\delta \text{CCC}$ (50)
-	-	420	403	<1	<1	$\tau \text{C3-C4-C5-C6}$ (78)
-	-	382	367	1	1	$\delta \text{N11C1C2}$ (61)
-	-	345	331	14	1	$\tau \text{NH}_2$ (93)
-	353 (2)	339	325	1	4	$\delta \text{C4C14C16}$ (58)
-	283 (3)	274	263	5	1	$\gamma \text{C14-C3-C5-C4}$ (75)
-	216 (3)	193	185	5	<1	$\delta \text{C3C4C5}$ (75)
-	114 (51)	141	135	0	<1	$\tau \text{CH}_3$ (91)
-	90 (30)	10	10	1	1	$\tau \text{C2-C3-C4-C5}$ (72)
-	69 (26)	69	66	4	<1	$\tau \text{C16-C14-C4-C3}$ (88)

<sup>a</sup> sh, shoulder; s, strong; w, weak; m, medium; v, very.

<sup>b</sup> Relative band heights in parentheses.

<sup>c</sup> Calculated at B3LYP/6-311++G(d,p) level of theory. IR intensities are shown in parenthesis.

<sup>d</sup>  $\nu$ : stretching,  $\delta$ : in-plane deformation,  $\gamma$ : out-of-plane deformation,  $\rho$ : rocking,  $\omega$ : wagging,  $\tau$ : twisting,  $\tau$ : torsion modes.

<sup>e</sup> See Fig. 2 for the atoms numbering scheme.

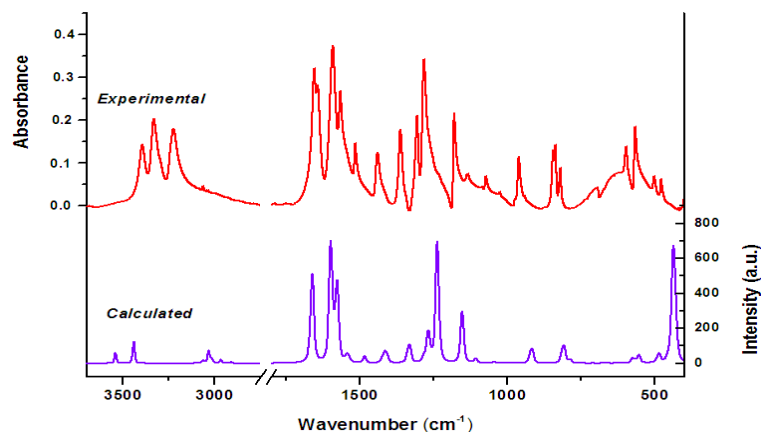


**Fig. 8:** Experimental and Theoretical IR Spectra of PAAP. Top: IR Spectrum of the Substance in Solid State Measured at RT; Bottom: Theoretical IR Spectrum Calculated at B3LYP/6-311++G(d, p) Level.

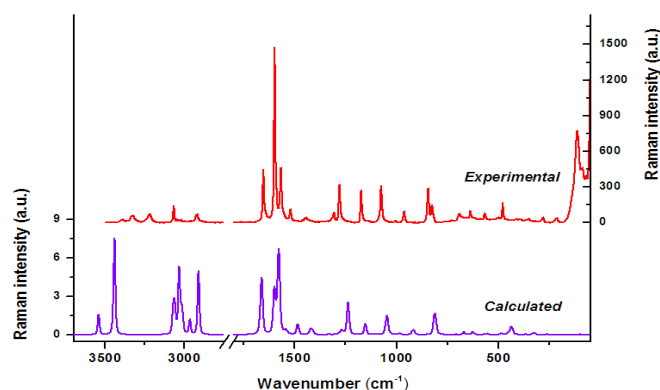


**Fig. 9:** Experimental and Theoretical Raman Spectra of PAAP. Top: Raman Spectrum of the Substance in Solid State Measured at RT; Bottom: Theoretical Raman Spectrum Calculated at B3LYP/6-311++G (d, p) Level.

### 3.5.1. Assignment of bands

**NH<sub>2</sub> vibrations:** The NH<sub>2</sub> group gives rise to the six internal modes of vibrations as: anti-symmetric and symmetric stretching, symmetric deformation, rocking, wagging and the torsional modes. The medium intensity band located at 3332 cm<sup>-1</sup> in the IR spectrum (3329 cm<sup>-1</sup> in Raman) is assigned to the NH<sub>2</sub> anti-symmetric stretching vibration. The medium intensity band located at 3226 cm<sup>-1</sup> in the IR spectrum and the strong band at 3220 cm<sup>-1</sup> in Raman are assigned to the NH<sub>2</sub> symmetric stretching mode. As was discussed previously, the formation of intermolecular N-H...O and LP N...H-N hydrogen bonding interactions are responsible for the impressive red-shift and strong intensification of the anti-symmetric and symmetric ν(NH<sub>2</sub>) normal modes as compared with related molecules [44]. These frequencies and ratio of intensities of the two bands are in accordance with calculations and they are characteristic of NH<sub>2</sub> stretching modes. In addition, the infrared spectrum shows absorption at 1641 cm<sup>-1</sup>, with strong intensity, which is tentative assigned to the NH<sub>2</sub> bending mode. Counterpart signal appears in the Raman spectrum at 1641 cm<sup>-1</sup>. The computed value for this mode is predicted to be 1663 cm<sup>-1</sup> at B3LYP/6-311++G(d,p) approximation. The very weak bands at 1025 and 478 cm<sup>-1</sup> in the IR spectrum are assigned to the NH<sub>2</sub> rocking and wagging modes, respectively. These frequency values and the relative intensities are in very good agreement with the computed ones, as showed in Table 6.

**CH<sub>3</sub> vibrations:** The anti-symmetric and symmetric stretching modes of methyl groups generally appear in the frequency range 3100 - 2880 cm<sup>-1</sup>. The very weak band located at 2977 cm<sup>-1</sup> in the IR spectrum is assigned to the CH<sub>3</sub> anti-symmetric stretching mode. The Raman spectrum shows a weak band at 2921 cm<sup>-1</sup> which is tentatively assigned to the CH<sub>3</sub> symmetric stretching mode. The anti-symmetric CH<sub>3</sub> deformation modes are observed as weak bands at 1439 and 1443 cm<sup>-1</sup> in the IR and Raman spectra, respectively. The medium intensity band at 1361 cm<sup>-1</sup> in the IR spectrum is assigned to the CH<sub>3</sub> symmetric bending mode. The band located at 114 cm<sup>-1</sup> in the Raman spectrum is assigned to the CH<sub>3</sub> torsional mode, in accordance with the computed value (141 cm<sup>-1</sup>).

**C=O vibrations:** Carbonyl group vibrations in ketones are the best characteristic bands in vibrational spectra, and for this reason, such bands have been the subject of extensive studies [45]. The intensity of these bands can increase because of conjugation, therefore, leads to the intensification of the Raman lines as well as the increased infrared band intensities. The C=O stretching vibrations in ketones are expected in the region 1680-1715 cm<sup>-1</sup> [45] and it is very sensitive to conformational properties as well as intra/intermolecular interactions. In this work, the C=O stretching mode for the title compound is observed as a strong band at 1652 cm<sup>-1</sup> in the IR spectrum and at 1651 cm<sup>-1</sup> in Raman. The frequency calculated for this mode is 1729 cm<sup>-1</sup>. In 4-hydroxy acetophenone, this mode is observed at 1656 cm<sup>-1</sup> in the Raman spectrum [46] but in 2,4-difluoro acetophenone and 3-aminoacetophenone the C=O vibrational mode is observed at 1692 and 1668 cm<sup>-1</sup>, respectively [3], [44].

**C-H vibrations:** For all aromatic compounds, the C-H stretching vibrations are observed in the frequency region 3250-3000 cm<sup>-1</sup>. The bands located at 3064 and 3048 cm<sup>-1</sup> in the IR spectrum (3067 and 3047 cm<sup>-1</sup> in Raman) are assigned to the C-H stretching mode. These bands have been predicted in the range 3197-3159 cm<sup>-1</sup> in calculations performed at B3LYP/6-311++G(d,p) level of approximation (See Table 6). The IR bands located at 1514, 1133, 1085 cm<sup>-1</sup> in the IR spectrum and at 1518 and 1137 cm<sup>-1</sup> in Raman are assigned to the C-H in-plane bending mode as reported in Table 6. The C-H out-of-plane bending modes are strongly coupled vibrations and generally appear in the region 960-600 cm<sup>-1</sup> [31], [32], [47-50]. The IR bands observed at 874, 836 and 819 cm<sup>-1</sup> in the IR spectrum (825 cm<sup>-1</sup> in Raman) confirm the presence of C-H out-of-plane bending vibrations in accordance with the values predicted from calculations and reported in literature [31], [32], [47-50].

**C-N, C-C and ring vibrations:** The strong band located at 1281 cm<sup>-1</sup> (1279 cm<sup>-1</sup> in Raman) is assigned to the C-N stretching mode with 51% of PED contribution, in agreement with the computed value of 1318 cm<sup>-1</sup> and with reported data for different species [45]. In accordance with PED analysis, this mode appears strongly coupled with the in-plane CCH bending modes of the phenyl ring. The ring C-C stretching vibrations occur in the region 1650-1000 cm<sup>-1</sup>. The ring C-C stretching bands appear in the IR spectrum at 1589, 1564, 1305, 1178 and 1072 cm<sup>-1</sup> (1596, 1564, 1306, 1172 and 1074 cm<sup>-1</sup> in Raman). The observed and calculated C-C-C in-plane and out-of-plane bending modes are presented in Table 6 along their assignment. These results are in accordance with the literature data [31,32, 47-50] and with values obtained by calculation

## 4. Conclusions

In this work, a complete structural, vibrational and electronic investigation along with FTIR, Raman, UV-visible, NBO and AIM approach of 4-aminoacetophenone have been carried out with B3LYP method and different basis sets. The calculated IR and Raman spectra are compared with the experimental data. A complete assignment of the observed bands was possible from the calculated normal modes of vibration. The molecular geometrical parameters have been calculated and correlated with the XRD data reported for the title compound. The calculated geometrical parameters show a very good agreement with the structure reported previously. The stability of the molecule arising from hyper-conjugative interactions and charge delocalization has been evaluated by means the NBO analysis. The TD-DFT calculation assisted the assignment of electronic transitions observed in the UV-visible absorption spectrum. NBO and AIM calculations

indicate that the intermolecular interactions observed in title compound are weak hydrogen bonds. The Hirshfeld surface analysis revealed that the H···H interactions comprise the majority of interactions. Shape index and Curvedness were useful to visualize the  $\pi$ -stacking interactions in the molecule, not reported previously. Finally, the enrichment ratios derived from the Hirshfeld surface analysis allowed us to quantify the likelihood of the main intermolecular contacts to form the crystal packing in PAAP. The analysis of the Hirshfeld surfaces and their 2D fingerprint plots provide useful information that cannot be obtained from conventional crystal packing diagrams or by detailed consideration of close intermolecular contacts. These tools are very important complements to the more traditional means of discussing, comparing and elucidating patterns in intermolecular interactions in crystalline solids.

## Acknowledgments

Authors thank CIUNT (Project D542/2), CONICET (PIP 0205) and ANPCyT (PICT-2013-0697 and PICT-2016-0226) for financial support. A.D.S. and M.R. thank CONICET for fellowships. A.B.A. and D.M.G. are members of the Research Career of CONICET.

## Supplementary material

Dipolar moment vector for PAAP at B3LYP/6-311++G(d,p) level (Figure S1), Optimized molecular structure of a dimer structure of PAAP calculated at B3LYP/6-311++G(d,p) level of theory (Figure S2), Molecular graph of 4-aminoacetophenone molecule calculated at B3LYP/6-311++G(d,p) approximation using AIM program (Figure S3), AIM Molecular graph of a dimer structure of PAAP (Figure S4), MEP plot for PAAP computed at B3LYP/6-311++G(d,p) approximation (Figure S5), Total atomic charges obtained using NPA approach, computed at B3LYP/6-311++G(d,p) approximation (Table S1), Enrichment ratios Exy of the main intermolecular interactions of PAAP (Table S2).

## References

- [1] Griffin, R.N. (1968). Phosphorescence of aromatic ketones in low-temperatures glasses, *Photochem. Photobiol.*, 7, 159-173. <https://doi.org/10.1111/j.1751-1097.1968.tb08003.x>.
- [2] Lutz, H., Duval, M.C., Breheret, E., Lindqvist, L. (1972), Solvent effects on acetophenone photoreduction studied by laser photolysis, *J. Phys. Chem.*, 76, 821-822. <https://doi.org/10.1021/j100650a004>.
- [3] Parimala, K., Balachandran, V. (2013), Structural study, NCA, FT-IR, FT-Raman spectral investigations, NBO analysis and thermodynamic properties of 2',4'-difluoroacetophenone by HF and DFT calculations, *Spectrochim. Acta A*, 110, 269-284. <https://doi.org/10.1016/j.saa.2013.03.058>.
- [4] P.M. Sivakumar, G. Sheshayan, M. Doble, (2008), Experimental and QSAR of Acetophenones as Antibacterial Agents, *Chem. Biol. Drug Des.* 72, 303-313. <https://doi.org/10.1111/j.1747-0285.2008.00702.x>.
- [5] A.M. Balan, O. Florea, C. Moldoveanu, G. Zbancioc, D. Iurea, I.I. Mangalagiu, (2009) Diazinium salts with dihydroxyacetophenone skeleton: syntheses and antimicrobial activity, *Eur. J. Med. Chem.* 44, 2275-2279. <https://doi.org/10.1016/j.ejmech.2008.06.017>.
- [6] V.P. Singh, S. Singh, A. Katiyar, (2009), Synthesis, physico-chemical studies of manganese (II), cobalt (II), nickel (II), copper (II) and zinc (II) complexes with some p-substituted acetophenone benzoylhydrazones and their antimicrobial activity, *J. Enzyme Inhib. Med. Chem.* 24, 577-88. <https://doi.org/10.1080/14756360802318662>.
- [7] V.P. Singh, A. Katiyar, S. Singh. (2008), Synthesis, characterization of some transition metal (II) complexes of acetone p-amino acetophenone salicyloyl hydrazone and their anti-microbial activity, *Biometals* 21, 491-501. <https://doi.org/10.1007/s10534-008-9136-9>.
- [8] H.Z. Wei, L.C. Wing, H.L. Yuan, S.S. Yan, C.L. Yong, H.Y. Chi, (1997), Synthesis of Hydroxyflavanones from Substituted Acetophenones and Benzaldehydes in the Presence of Silica Gel, Boric Acid and Piperidine Heterocycles. 45, 71-75. <https://doi.org/10.3987/COM-96-7611>.
- [9] M.J. Climent, A. Corma, S. Iborra, A. Velty, (2004), Activated hydroxaldehydes as catalysts for the synthesis of chalcones of pharmaceutical interest. *J. Catal.*, 221,474-. <https://doi.org/10.1016/j.jcat.2003.09.012>.
- [10] M. Sittig, *Handbook of Toxic and Hazardous Chemicals and Carcinogens*, second ed., Noyes Publications, Park Ridge, NJ, 1985.
- [11] K.C. Medhi, (1977), The vibrational spectra of 2-, 3-and 4- acetylpyridine, *Ind. J. Phys.* 51A, 399.
- [12] A. Gambi, S. Gioggianni, A. Passerini, R. Visinoni, S. Ghersetti, (1980), Infrared studies of acetophenone and its deuterated derivatives, *Spectrochim. Acta* 36A, 871-878. [https://doi.org/10.1016/0584-8539\(80\)80036-5](https://doi.org/10.1016/0584-8539(80)80036-5).
- [13] P. Sett, S. Chattopadhyay, P.K. Mallick, (2000), Normal coordinate analyses of three isomeric acetylpyridines and acetophenone *J. Raman Spectrosc.* 31, 177-184. [https://doi.org/10.1002/\(SICI\)1097-4555\(200003\)31:3<177::AID-JRS509>3.0.CO;2-K](https://doi.org/10.1002/(SICI)1097-4555(200003)31:3<177::AID-JRS509>3.0.CO;2-K).
- [14] M.J. Frisch, J.A. Pople, J.S. Binkley, J. Chem. Phys. 80 (1984) 3265. M.J. Frisch, G.W. Trucks, H.B. Schlegel, G.E. Scuseria, M.A. Robb, J.R. Cheeseman, J.A. Montgomery Jr., T. Vreven, K.N. Kudin, J.C. Burant, J.M. Millam, S.S. Iyengar, J. Tomasi, V. Barone, B. Mennucci, M. Cossi, G. Scalmani, N. Rega, G.A. Petersson, H. Nakatsuji, M. Hada, M. Ehara, K. Toyota, R. Fukuda, J. Hasegawa, M. Ishida, T. Nakajima, Y. Honda, O. Kitao, H. Nakai, M. Klene, X. Li, J.E. Knox, H.P. Hratchian, J.B. Cross, C. Adamo, J. Jaramillo, R. Gomperts, R.E. Stratmann, O. Yazyev, A.J. Austin, R. Cammi, C. Pomelli, J.W. Ochterski, P.Y. Ayala, K. Morokuma, G.A. Voth, P. Salvador, J.J. Dannenberg, V.G. Zakrzewski, S. Dapprich, A.D. Daniels, M.C. Strain, O. Farkas, D.K. Malick, A.D. Rabuck, K. Raghavachari, J.B. Foresman, J.V. Ortiz, Q. Cui, A.G. Baboul, S. Clifford, J. Cioslowski, B.B. Stefanov, G. Liu, A. Liashenko, P. Piskorz, I. Komaromi, R.L. Martin, D.J. Fox, T. Keith, M.A. Al-Laham, C.Y. Peng, A. Nanayakkara, M. Challacombe, P.M.W. Gill, B. Johnson, W. Chen, M.W. Wong, C. González, J.A. Pople, Gaussian 03, revision C.02, Gaussian Inc., Wallingford, CT, 2004.
- [15] A.D. Becke, (1993), Density-functional thermochemistry. III. The role of exact exchange J., *Chem. Phys.* 98, 5648-5652. <https://doi.org/10.1063/1.464913>.
- [16] C. Lee, W. Yang, R.G. Parr, (1988), Development of the Colle-Salvetti correlation-energy formula into a functional of the electron density, *Phys. Rev. B* 37, 785. <https://doi.org/10.1103/PhysRevB.37.785>.
- [17] M.J. Frisch, A.B. Nielsen, A.J. Holder, Gaussview User Manual, Gaussian, Pittsburgh, 2008.
- [18] M.H. Jamróz, (2013), Vibrational energy distribution analysis (VEDA): scopes and limitations, *Spectrochim. Acta A* 114, 220-230. <https://doi.org/10.1016/j.saa.2013.05.096>.
- [19] R.F.W. Bader, *Atoms in Molecules*, A Quantum Theory, Claderon Press, Oxford, 1990.
- [20] V. Arjunan, L. Devi, R. Subbalakshmi, T. Rani, S. Mohan. (2014), Synthesis, vibrational, NMR, quantum chemical and structure-activity relation studies of 2-hydroxy-4-methoxyacetophenone, *Spectrochim. Acta A*, 130, 164-177. <https://doi.org/10.1016/j.saa.2014.03.121>.
- [21] E.D. Glendening, J.K. Badenhop, A.D. Reed, J.E. Carpenter, F.F. Weinhold, Theoretical Chemistry Institute, University of Wisconsin, Madison, WI, 1996.
- [22] D.M. Chipman, (2000), Reaction field treatment of charge penetration *J. Chem. Phys.* 112, 5558. <https://doi.org/10.1063/1.481133>.
- [23] J.J. McKinnon, D. Jayatilaka, M.A. Spackman, (2007), Towards quantitative analysis of intermolecular interactions with Hirshfeld surfaces, *Chem. Commun.*, 37, 3814-3816. <https://doi.org/10.1039/b704980c>.
- [24] M.A. Spackman, D. Jayatilaka, (2009), Hirshfeld Surface Analysis, *CrystEngComm* 11, 19-32. <https://doi.org/10.1039/B818330A>.

- [25] J.J. McKinnon, M.A. Spackman, A.S. Mitchel. (2004), Novel tools for visualizing and exploring intermolecular interactions in molecular crystals. *Acta Crystallogr.* 60B, 627-68. <https://doi.org/10.1107/S0108768104020300>.
- [26] S.K. Wolf, D.J. Grimwood, J.J. McKinnon, M.J. Turner, D. Jayatilaka, M.A. Spackman, *CrystalExplorer* (version 3.1), University of Western, Australia, 2012.
- [27] M. Haisa, S. Kashino, T. Yuasa, K. Akigawa, (1976), Topochemical studies. IX. The crystal and molecular structure of *p*-aminoacetophenone *Acta Cryst. B* 32 (1976) 1326-1328. <https://doi.org/10.1107/S0567740876012600>.
- [28] A. Saeed, M. Ifzan Arshad, M. Bolte, A.C. Fantoni, Z. Y. Delgado Espinoza, M.F. Erben, (2016), On the roles of close shell interactions in the structure of acyl-substituted hydrazones: An experimental and theoretical approach., *Spectrochim. Acta A* 157, 138-145. <https://doi.org/10.1016/j.saa.2015.12.026>.
- [29] R.F.W. Bader, *Atoms in Molecules, A Quantum Theory*, Claderon Press, Oxford, 1990.
- [30] H. Roohi, A. Ebrahimi, F. Alirezapoor, M. Hadealirezahi, (2005), AIM and NBO analyses of N–N rotational barrier in monocyclic nitrosamine compounds *Chem. Phys. Lett.* 409, 212-218. <https://doi.org/10.1016/j.cplett.2005.05.022>.
- [31] M. Rocha, A. Di Santo, J.M. Arias, D.M. Gil, A. Ben Altabef, (2015) Ab-initio and DFT calculations on molecular structure, NBO, HOMO-LUMO study and a new vibrational analysis of 4-(Dimethylamino) Benzaldehyde., *Spectrochim. Acta A* 136, 635-643. <https://doi.org/10.1016/j.saa.2014.09.077>.
- [32] D.M. Gil, M.E. Defonsi Lestard, O. Estévez- Hernández, J. Duque, E. Reguera (2015), Quantum chemical studies on molecular structure, spectroscopic (IR, Raman, UV-Vis), NBO and HOMO-LUMO analysis of 1-benzyl-3-(2-furoyl) thiourea, *Spectrochim. Acta A* 145, 553-562. <https://doi.org/10.1016/j.saa.2015.02.071>.
- [33] D.M. Gil, O.E. Piro, G.A. Echeverría, M. E. Tuttolomondo, A. Ben Altabef (2013), Layered crystal structure, conformational and vibrational properties of 2,2,2-trichloroethoxysulfonamide: an experimental and theoretical study, *Spectrochim. Acta A* 116, 122-131. <https://doi.org/10.1016/j.saa.2013.07.013>.
- [34] U. Koch, P.L.A. Popelier, (1995), Characterization of C-H-O Hydrogen Bonds on the Basis of the Charge Density *J. Phys. Chem.* 99, 9747-9754. <https://doi.org/10.1021/j100024a016>.
- [35] E. Espinosa, E. Molins, C. Lecomte, (1998), Hydrogen bond strengths revealed by topological analyses of experimentally observed electron densities *Chem. Phys. Lett.* 285, 170-173. [https://doi.org/10.1016/S0009-2614\(98\)00036-0](https://doi.org/10.1016/S0009-2614(98)00036-0).
- [36] I. Rozas, I. Alkorta, J. Elguero, (2011), Behavior of Ylides Containing N, O, and C Atoms as Hydrogen Bond Acceptors, *J. Am. Chem. Soc.* 122, 11154-11161. <https://doi.org/10.1021/ja0017864>.
- [37] E. Scrocco, J. Tomasi, (1979), *Electronic Molecular Structure, Reactivity and Intermolecular Forces: An Euristic Interpretation by Means of Electrostatic Molecular Potentials* *Adv. Quantum Chem.*, 11, 115-193. [https://doi.org/10.1016/S0065-3276\(08\)60236-1](https://doi.org/10.1016/S0065-3276(08)60236-1).
- [38] F.J. Luque, J.M. Lopez, M. Orozco, (2000), Perspective on “Electrostatic interactions of a solute with a continuum. A direct utilization of ab initio molecular potentials for the prevision of solvent effects” *Theor. Chem. Acc.* 103, 343-345. [https://doi.org/10.1007/978-3-662-10421-7\\_56](https://doi.org/10.1007/978-3-662-10421-7_56).
- [39] C. Jelsch, K. Ejsmont, L. Huder, (2014), The enrichment ratio of atomic contacts in crystals, an indicator derived from the Hirshfeld surface analysis, *IUCrJ* 1, 119-128. <https://doi.org/10.1107/S2052252514003327>.
- [40] M. Govindarajan, S. Periandi, K. Carthigayen, (2012), FT-IR and FT-Raman spectra, thermo dynamical behavior, HOMO and LUMO, UV, NLO properties, computed frequency estimation analysis and electronic structure calculations on  $\alpha$ -bromotoluene *Spectrochim. Acta A* 97, 411-422. <https://doi.org/10.1016/j.saa.2012.06.028>.
- [41] M. Govindarajan, M. Karabacak, (2012), Spectroscopic properties, NLO, HOMO-LUMO and NBO analysis of 2,5-Lutidine *Spectrochim. Acta A* 96, 421-435. <https://doi.org/10.1016/j.saa.2012.05.067>.
- [42] C. Ravikumar, I.H. Joe, V.S. Jayakumar, (2008), Charge transfer interactions and nonlinear optical properties of push–pull chromophore benzaldehyde phenylhydrazone: A vibrational approach., *Chem. Phys. Lett.* 460 552-558. <https://doi.org/10.1016/j.cplett.2008.06.047>.
- [43] A. Fu, D. Du, Z. Zhou, (2003), Density functional theory study of vibrational spectra of acridine and phenazine *Spectrochim. Acta A* 59, 245-253. [https://doi.org/10.1016/S1386-1425\(02\)00169-5](https://doi.org/10.1016/S1386-1425(02)00169-5).
- [44] M.K. Subramanian, P.M. Anbarasan, V. Ilangovan, S. Moorthy Babu, (2008), FT-IR, NIR-FT-Raman and gas phase infrared spectra of 3-aminoacetophenone by density functional theory and ab initio Hartree–Fock calculations *Spectrochim. Acta A* 71, 59-67. <https://doi.org/10.1016/j.saa.2007.11.013>.
- [45] D. Lin-Vien, N.B. Colthup, W.G. Fateley, J.G. Grasselli, *The Handbook of Infrared and Raman Characteristic Frequencies of Organic Molecules*, Academic Press, 1991.
- [46] D. Sajan, I.H. Joe, V.S. Jayakumar, (2006), NIR-FT Raman, FT-IR and surface-enhanced Raman scattering spectra of organic nonlinear optic material: *p*-hydroxy acetophenone, *J. Raman Spectrosc.* 37, 508-519. <https://doi.org/10.1002/jrs.1424>.
- [47] V. Arjunan, M. Kalaivani, S. Senthikumari, S. Mohan, (2013), Vibrational, NMR and quantum chemical investigations of acetoacetanilide, 2-chloro-acetoacetanilide and 2-methylacetoacetanilide, *Spectrochim. Acta A* 115, 154-174. <https://doi.org/10.1016/j.saa.2013.06.003>.
- [48] L.P. Avendaño Jiménez, G.A. Echeverría, O.E. Piro, S.E. Ulic, J.L. Jios, (2013), Vibrational, electronic, and structural properties of 6-nitro- and 6-amino-2-trifluoromethylchromone: an experimental and theoretical study, *J. Phys. Chem. A* 117, 2169-2180. <https://doi.org/10.1021/jp312683s>.
- [49] C. Sridevi, G. Shanthi, G. Velraj, (2012), Structural, vibrational, electronic, NMR and reactivity analyses of 2-amino-4H-chromene-3-carbonitrile (ACC) by ab initio HF and DFT calculations. *Spectrochim. Acta A* 89, 46-54. <https://doi.org/10.1016/j.saa.2011.12.050>.
- [50] E. Lizarraga, D.M. Gil, G.A. Echeverría, O.E. Piro, C.A.N. Catalán, A. Ben Altabef, (2014), Synthesis, crystal structure, conformational and vibrational properties of 6-acetyl-2,2-dimethyl-chromane. *Spectrochim. Acta A* 127, 74-84. <https://doi.org/10.1016/j.saa.2014.02.035>.